ADVANCED FUNCTIONAL MATERIALS

A Flexible and Biomimetic Olfactory Synapse with Gasotransmitter-Mediated Plasticity

Yuping Deng, Mingyou Zhao, Yuan Ma, Shangbin Liu, Mingda Liu, Boyu Shen, Rongfeng Li, He Ding, Huanyu Cheng, Xing Sheng, Wangyang Fu, Zehui Li, Milin Zhang, and Lan Yin*

Neuromorphic electronics has demonstrated great promise in mimicking the sensory and memory functions of biological systems. However, synaptic devices with desirable sensitivity, selectivity, and operational voltage imitating the olfactory system have rarely been reported. Here, a flexible and biomimetic olfactory synapse based on an organic electrochemical transistor (OECT) coupled with a breath-figure derived porous solid polymer electrolyte (SPE) is proposed. The device demonstrates excellent sensitivity with a ppb-level response limit and desirable selectivity toward hydrogen sulfide (H_2S) over other gases, and successfully achieves wireless real-time detection of excessive concentration of H_2S from rotten eggs. H_2S-mediated synaptic plasticity is accomplished with the device and typical synaptic behaviors are realized, including short-term memory (STM), long-term memory (LTM), transition from STM to LTM, etc., enabling the imitation of potential cumulative damages upon H_2S exposure. The proposed device paves new ways toward next-generation olfactory systems capable of sensing and memorizing functionalities mimicking neurobiological systems, offering critical materials strategies to accomplish intelligent artificial sensory systems.

1. Introduction

Human brain is an incredibly efficient computing system which is composed of $\approx 10^{11}$ neurons and $\approx 10^{15}$ synapses.[1] In virtue of parallel interconnected structure, biological computing is able to deal with a wealth of complex information by combining signal processing, memory and learning together in a power-efficient manner.[2] Inspired by human brain, artificial sensory systems using neuromorphic electronics aim to response to external stimuli such as pressure, light, smell, etc., in ways emulating the behavior of neural systems including perception and memory functions.[3] In biological systems, information is transferred from the synapses of pre-neuron to those of the post-neuron through conveying electrical or chemical signals.[1] Changes in

Y. Deng, B. Shen, L. Yin
School of Materials Science and Engineering
The Key Laboratory of Advanced Materials of Ministry of Education
State Key Laboratory of New Ceramics and Fine Processing
Center for Flexible Electronics Technology
Tsinghua University
Beijing 100084, China
E-mail: lanyin@tsinghua.edu.cn

M. Zhao
College of Engineering
Peking University
Beijing 100084, China

Y. Ma, M. Zhang
Department of Electronic Engineering
Tsinghua University
Beijing 100084, China

S. Liu, H. Cheng
Department of Engineering Science and Mechanics
The Pennsylvania State University
University Park, PA 16802, USA

M. Liu, W. Fu
School of Materials Science and Engineering
Tsinghua University
Beijing 100084, China

R. Li
Beijing Institute of Collaborative Innovation
Beijing Siweizhigan Co., Ltd
Beijing 100084, China

H. Ding
Beijing Engineering Research Center of Mixed Reality
and Advanced Display
School of Optics and Photonics
Beijing Institute of Technology
Beijing 100084, China

X. Sheng
Department of Electronic Engineering
Beijing National Research Center for Information Science
and Technology
Institute for Precision Medicine
Center for Flexible Electronics Technology, and IDG/McGovern
Institute for Brain Research
Tsinghua University
Beijing 100084, China

Z. Li
State Key Laboratory for Mesoscopic Physics
Frontiers Science Center for Nano-optoelectronics
School of Physics
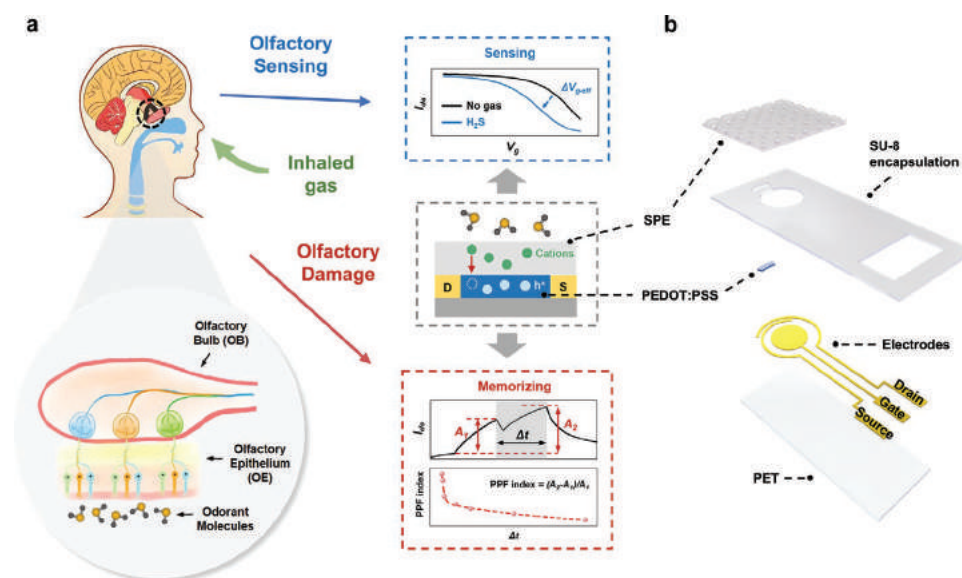Peking University
Beijing 100084, China

Figure 1. Schematic illustration of the flexible and biomimetic olfactory synapse based on organic electrochemical transistors (OECTs). a) Synaptic devices mimicking olfactory sensing and potential damage toward gasotransmitter H_2S. Schematic illustration of the working principle of the synaptic device (grey dashed line box). The shift of transfer curves of OECTs upon the exposure to H_2S molecules enables gas sensing (blue dashed line box). The memorizing behavior of the synaptic device allows the imitation of olfactory damage due to the overexposure of H_2S (red dashed line box). b) Device structure of the biomimetic olfactory synapse, consisting of a layer of porous solid polymer electrolyte (SPE), an SU-8 encapsulation layer, a patterned PEDOT:PSS channel, drain, source and gate electrodes, and a flexible PET substrate.

the efficiency of the connections between neurons are known as synaptic plasticity, which is believed to be the underpinning of learning and memory.[4] The implementation of synaptic behaviors at the device level enables artificial synapses to imitate neurobiological behavior, such as electronic skins (E-skins) that can simultaneously realize tactile perception and memory functionalities,[5] artificial optic-neural synapses to realize visual self-adjusting in real-life scenes,[6] bimodal synapses that are capable of cross-modal recognition and imagination,[7] and transistor networks with ionic polymeric electrolytes that exhibit pain-perception abilities.[8]

Olfactory system, another important sensory platform, enables vital recognition of numerous odor molecules, endowing human with abilities to sense surrounding environments, evaluate food and identify potential dangers.[9] However, the development of synaptic olfactory devices is still at the early stage, probably due to the complicated olfactory sensing system. The biological olfactory recognition process starts with the chemical interactions between inhaled odorants and the olfactory receptors of peripheral sensory neurons in olfactory epithelium (OE) which lies in the dorsal nasal cavity (**Figure 1a**).[10] The resulting electrical signals are transmitted to neighboring neurons of the main olfactory bulb (OB) where information is pre-encoded before transferred to olfactory cortex for further deciphering.[11] The OB plays an important role in olfactory sensory system as it exhibits neural plasticity that is critical for olfactory learning and memorizing.[12] Efforts to mimic olfactory sensory functions have inspired a variety of gas sensors such as electronic noses (E-noses) with excellent odorant identification and differentiation with high accuracy.[13] However, synaptic olfactory systems that integrate olfactory perception and memory functionalities have rarely been proposed. Only a few works on

olfactory synapse toward nitrogen dioxide (NO_2) and ammonia (NH_3) were reported.[14] Nevertheless, limited sensitivity and selectivity or high operation voltages of available devices could constrain potential applications.

Recently, organic electrochemical transistors (OECTs) have emerged as artificial synaptic devices with efficient ion-to-electron transduction, low operation voltage (≤1 V) and excellent biocompatibility.[15] The conducting polymer poly(3,4-ethylenedioxythiophene) doped with poly(styrene sulfonate) (PEDOT:PSS) represents a typical material for OECTs. As voltage-controlled ion injection and extraction within the PEDOT:PSS channel is identical to the release and absorption of neurotransmitters in the synaptic cleft, OECTs based on PEDOT:PSS have been successfully demonstrated for neuromorphic functions including synaptic plasticity,[16] global phenomena,[17] and neuromorphic computing.[18] PETDOT:PSS can therefore serve as a candidate material to build olfactory synaptic devices which has rarely been explored before.

Hydrogen sulfide (H_2S) is an endogenous gasotransmitter that has been involved in various physiological and pathological processes, including cytoprotection, vascular relaxation, and neuromodulation.[19] However, inhaled H_2S of abnormal concentrations is highly toxic that can pose a significant threat to human health. It is reported that low concentrations (e.g., an 8 h time-weighted average concentration of 5 ppm) of H_2S may lead to adverse health effects, and high concentrations (>100 ppm) may even lead to sudden death.[20] Although the pungent odor of H_2S at very low concentrations (≈ 25 ppb) is detectable by human nose, olfactory perception does not response well to long-term or excessive exposure due to olfactory fatigue often caused by the damages of epithelium receptors.[21] The cumulative adverse effects induced by frequent exposure to

H_2S cannot be recorded by most conventional H_2S gas sensors either, in which case electrical response fades away rapidly upon the removal of external stimuli.[14a] Hence, the development of artificial olfactory synapses capable of H_2S sensation and memory functionalities show great promise for next-generation olfactory electronics that could alarm potential accumulative influence of harmful gas species.

In this work, we propose a flexible biomimetic olfactory synapse based on a single OECT. By introducing a breath-figure derived porous solid polymer electrolyte (SPE), the device shows excellent sensitivity (ppb-level) toward H_2S over potential interfering gases as well as memory capability of accumulative effects. Gasotransmitter-mediated plasticity is successfully demonstrated by showing the transition from short-term memory (STM) to long-term memory (LTM) of the artificial olfactory synapse. The research sheds light on innovative strategies for future E-noses achieving both sensing and memorizing functionalities imitating neurobiological systems, which sets critical foundation to accomplish intelligent biomimetic olfactory sensory system and could be beneficial for health care.

2. Results

2.1. Device Structure of the Biomimetic Olfactory Synapse

In the biomimetic olfactory synapse, a breath-figure derived SPE functions as an artificial OE, and a PEDOT:PSS based OECT is used to emulate the OB (Figure 1a). The porous SPE is able to capture H_2S molecules from the environment, which modulates the doping state of PEDOT:PSS channel. The SPE enables the operation of OECT in gaseous environments and the elimination of potential swelling of PEDOT:PSS films in aqueous electrolytes. As shown in Figure 1a, the bio-synapse can sense the H_2S gas molecules by measuring the shift in the transfer curves [drain current (I_{ds}) versus gate voltage (V_g)], which is similar to the olfactory recognition process. Furthermore, the biomimetic olfactory synapse also demonstrates desirable gas-mediated plasticity to imitate the memory of olfactory damage due to the overexposure of H_2S, in which case gate voltage and gas molecules work as stimuli and I_{ds} represents the postsynaptic weight.

The layout of the proposed biomimetic olfactory synapse is shown in Figure 1b and the associated fabrication process is described in detail in the Methodology Section and **Figure 2**a. The device consists of a flexible polyethylene terephthalate (PET) substrate (≈125 μm), chromium (Cr)/gold (Au) (≈5 nm/80 nm) source, drain, and gate electrodes, a PEDOT:PSS channel (≈100 nm), an SU-8 passive layer (≈5 μm) only exposing the area of PEDOT:PSS, gate and electrical contacts, and a porous SPE (≈1 μm) comprising of poly(vinylidene fluoride-co-hexafluoropropylene) (PVDF-co-HFP) and ionic liquid (IL, 1-butyl-3-methylimidazolium bis[(trifluoromethyl)sulfonyl] imide, [BMIM][TFSI]). Specifically, the PEDOT:PSS channel has a dimension of length (L) 10 μm and width (W) 1000 μm, and the gate electrode has a radius of 1 mm. PEDOT:PSS, Cr/Au electrodes and the SU-8 layer are patterned by photolithography. A breath-figure method is used to fabricate the SPE layer where condensed water droplets in a humid environment

[relative humidity (RH) ≈60%] are used as sacrificial templates to produce microporous structure films as reported previously,[22] which could greatly enhance the effective area of gas interaction and improve device sensitivity as will be discussed later. By contrast, a dense SPE is also obtained by spin-coating in ambient circumstances (RH ≈25%) for comparison.

The SEM images of dense and porous SPE are given in Figure 2b,c respectively. Small PVDF-HFP spherical particles tend to form a flake-type morphology in the dense SPE (Figure 2b) while micropores are achieved in the porous SPE (Figure 2c). Figure 2d shows the XRD patterns of pure PVDF-HFP, dense and porous SPE, respectively. Characteristic peaks ≈18.7° and 20.2° are detected in pure PVDF-HFP, which indicates its semicrystalline nature.[23] However, with the addition of IL ([BMIM][TFSI]) into the PVDF-HFP polymer matrix, the crystalline peak of pure PVDF-HFP at 18.7° disappears and a broadened peak at ≈20° with reduced intensity is observed, indicating that [BMIM][TFSI] may function as a plasticizer and promote the amorphous phase in SPE.[24] Such amorphous regions are advantageous to enhance ionic conductivity through ion-hopping mechanism,[25] which could be beneficial to the electrical performance of OECTs[26] and will be discussed later. In addition, the XRD patterns in Figure 2d shows a broad peak near 12° in both dense and porous SPE films, which may be induced by the short-range ordering of IL at the polymer-IL interface.[27] The Fourier transform infrared spectroscopy (FTIR) spectra of pure PVDF-HFP, pure [BMIM][TFSI], porous and dense SPE in the region 600–3500 cm^{-1} are given in Figure 2e,f. The vibrational bands of pure polymer PVDF-HFP observed at 674.9, 771.7, and 812.4 cm^{-1} are due to the crystalline phase (α-phase), while the bands at 836.2 and 876.5 cm^{-1} are related to the amorphous phase (β-phase) of the polymer.[28] With the introduction of [BMIM][TFSI] in PVDF-HFP, α-phase related peaks get weaker and even disappear, while the peaks at 836.2 and 876.5 cm^{-1} associated with the amorphous phase remain prominent (porous and dense SPE in Figure 2e), which is consistent with the XRD results. The peaks at 1331.2 and 1349.6 cm^{-1}, and 3121.6 and 3157.8 cm^{-1} are the typical bands of $TFSI^-$ anions[28a,29] and C−H stretching vibrations of imidazolium cation ring,[30] respectively, which can be clearly identified in pure IL ([BMIM][TFSI]) and in both the porous and dense SPE, confirming the presence of IL in the SPE films (Figure 2f).

The electrical characteristics of OECTs with pure IL ([BMIM][TFSI]), dense and porous SPE are investigated and the results appear in Figure S1 (Supporting Information). Standard output characteristics are observed at the drain voltage (V_d) ranging from 0 to −0.6 V of five distinct V_g from 0 to 1.6 V with an interval of 0.4 V. The output curves in Figure S1a (Supporting Information) show a linear relationship between V_d and I_{ds} in the lower range of V_d, which indicates a desirable ohmic contact between Au electrodes and the PEDOT:PSS layer.[31] Devices with both dense and porous SPE exhibit the typical behavior of p-type OECTs working in a depletion mode (Figure S1a, Supporting Information), in which case voltage-controlled injection of [BMIM] cations from the SPE into the channel could result in the de-doping of the PEDOT:PSS.[26b,32] The possible reaction is as follows:
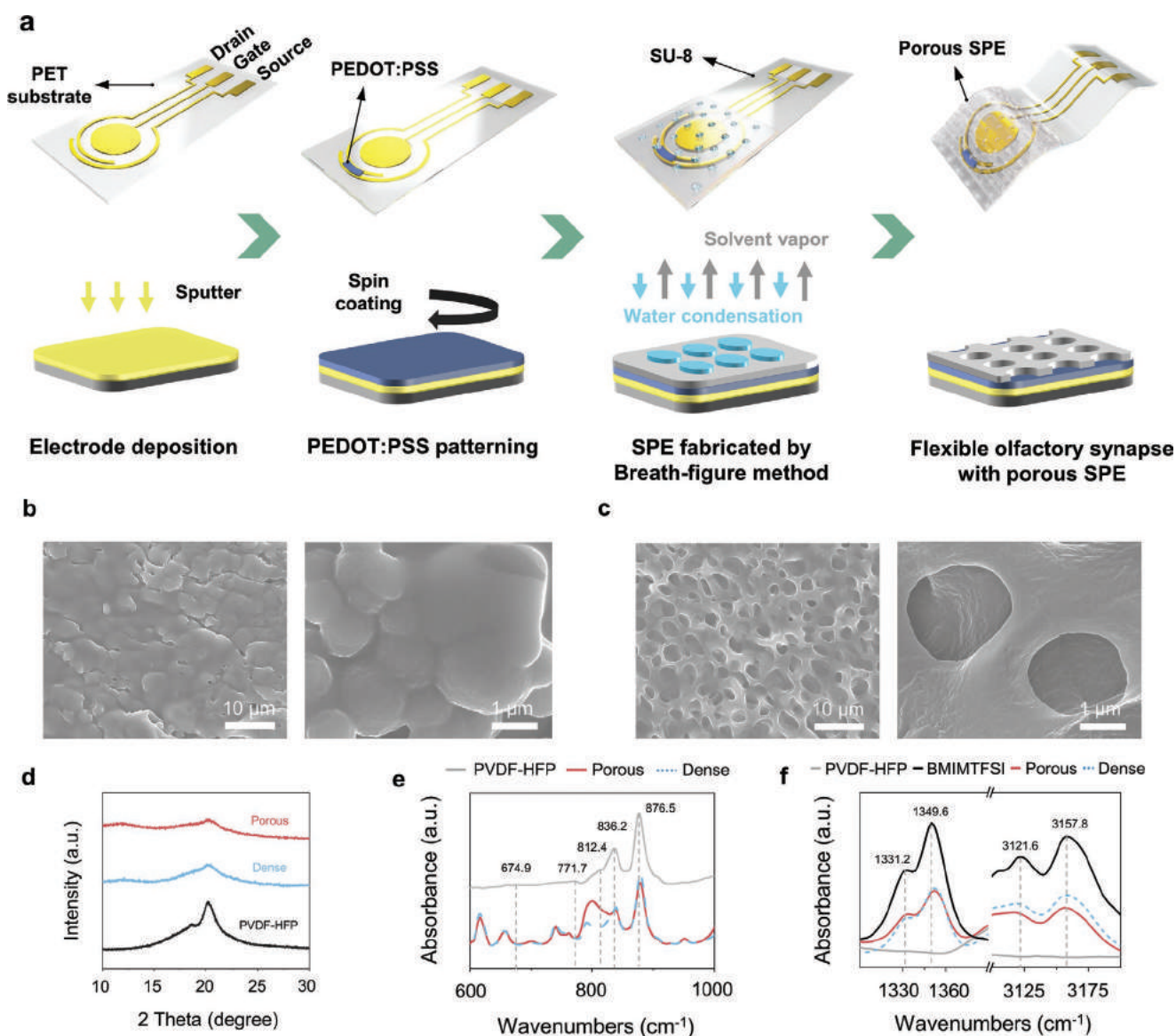
$$PEDOT^+:PSS^- + [BMIM]^+ \leftrightarrow PEDOT^0 + [BMIM]^+:PSS^- + h^+ \quad (1)$$

Figure 2. Fabrication schemes and characterizations of the porous solid electrolyte of the biomimetic olfactory synapse. a) Schematic illustration of the fabrication process though a breath-figure method. The fabrication process starts with the deposition of Au electrodes by magnetron sputtering on a PET substrate laminated on a PDMS coated glass substrate. PEDOT:PSS is patterned between the source and drain electrodes by photolithography. A layer of SU-8 serves as encapsulation exposing the channel, gate and electrode contacts. Porous solid polymer electrolyte (SPE) is fabricated on the device by the breath-figure method. The device is peeled off from the PDMS-coated glass to achieve a flexible biomimetic olfactory synapse. b) SEM images of dense SPE films at different magnifications. c) SEM images of porous SPE films at different magnifications. d) XRD patterns of PVDF-HFP, dense and porous SPE, respectively. e) FTIR spectra of PVDF-HFP, dense and porous SPE in the region of 600–1000 cm^{-1}. f, FTIR spectra of PVDF-HFP, BMIMTFSI, dense and porous SPE in the region of 1000–3500 cm^{-1}.

A typical transfer curve is also observed in OECTs with both dense and porous SPE (Figure S1b, Supporting Information). Corresponding transconductance ($g_m = \Delta I_{ds}/\Delta V_g$) is calculated and OECTs with both porous and dense SPE demonstrate desirable gating efficiency (Figure S1b, Supporting Information). By contrast, OECTs with pure [BMIM][TFSI] electrolyte shows the worst modulation performance (Figure S1a,b, Supporting Information), which may be due to the sluggish polarization response of pure IL as reported previously.[33] These results suggest that OECTs with SPE combining both IL and PVDF-HFP can greatly enhanced gating performance (Figure S1a,b, Supporting Information). The maximum transconductance ($g_{m,max}$)

is 1.88 and 1.54 mS for porous and dense SPE, respectively, which is comparable to the transconductance of OECTs operating with an aqueous electrolyte.[34] Gate leakage currents are given in Figures S1b and S2 (Supporting Information), and all devices demonstrate gate leakage currents lower than 50 nA.

2.2. Working Principle of the Olfactory Synapse

Figure 3 shows the operation mechanism of the biomimetic olfactory synapse. In the case of a biological synapse, signals are conveyed from presynaptic neurons to postsynaptic
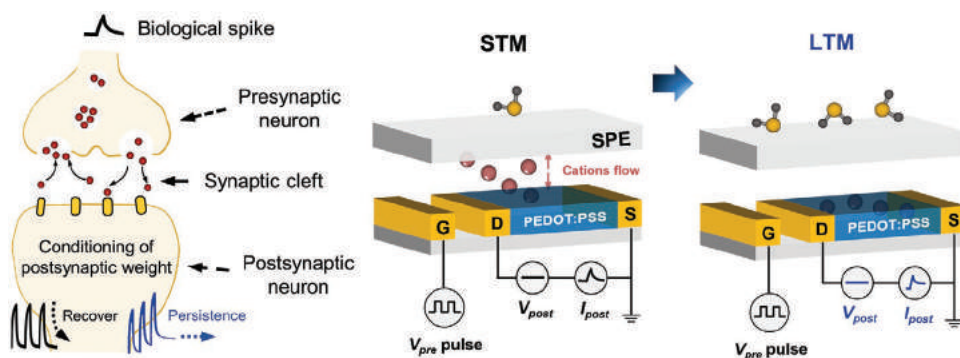
Figure 3. Mechanism of the biomimetic olfactory synapse with gasotransmitter-mediated plasticity. Schematic illustration of synaptic plasticity mediated by gasotransmitter mimicking biological synapses. In the biological synapse, short-term to long-term potentiation transition occurs when neurotransmitter molecules are released by exocytosis from the presynaptic cell and bound to receptors of the postsynaptic cell. In the artificial synapse, short-term to long-term potentiation transition occurs when excessive H_2S molecules are captured by the solid polymer electrolyte, which irreversibly drives cations from the electrolyte into the PEDOT:PSS channel.

neurons to realize basic functions in computation and memory. Synaptic plasticity denotes the conditioning of synaptic weights modulated by stimuli, and can be divided into short-term plasticity (STP) and long-term potentiation (LTP). STP occurs when a biological spike arrives at the presynaptic neuron and temporarily enhanced synaptic connection is achieved, which generally recovers to the initial state quickly. By contrast, repeated stimuli extend the persistence of the conditioning of postsynaptic weights and LTP is realized.

In the synaptic device, the gate electrode coupled with SPE in the biomimetic synapse is analogous to the presynaptic domain, and PEDOT:PSS channel between the drain and source electrodes is analogous to the postsynaptic domain. The release and uptake of neurotransmitters are emulated by chemical doping and de-doping of PEDOT:PSS via the injection and extraction of cations in the SPE, and the associated synaptic plasticity is regulated by H_2S and gate voltage pulses in a cross-modal way, which could be implemented to emulate the olfactory system including sensory, metabolism and cumulative damages toward H_2S.

When the biomimetic synapse is exposed under H_2S, [BMIM][TFSI] in the SPE could establish ionic associations with H_2S[35] which could help weaken electrostatic interactions between [BMIM]$^+$ cations and [TFSI]$^-$ anions and thus contribute to relaxed cluster formation and enhanced ion mobility.[36] The improved ion mobility in SPE could facilitate the gate modulation of OECTs (Equation (1)), which leads to additional cations [BMIM]$^+$ moving into the channel, de-doping PEDOT:PSS and thus reducing the channel current. These interactions set the foundation for sensing functionality toward H_2S. The FTIR measurement of SPE before and after H_2S exposure reveals almost the same spectra (Figure S3, Supporting Information), suggesting reversible interactions between the SPE and H_2S during the operation process, which is consistent with the reported reactions between IL and H_2S.[37] The corresponding hole mobility under different states can also be evaluated following the method reported previously,[38] and enhanced hole mobility in PEDOT:PSS channel upon the exposure to H_2S is observed (Figure S4, Supporting Information), which has been reported to be associated with the de-doping of PEDOT:PSS,[39] supporting the proposed sensing mechanism of the device toward H_2S.

Moreover, the doped cations in PEDOT:PSS channel are unable to diffuse back to the SPE immediately after the removal of gate pulses and H_2S due to slow ion relaxation resulting from large size cations in the SPE.[16a,40] These accumulated cations maintain the channel modulation state for a certain amount of time that could range from few seconds to a few minutes or even hours, depending on the concentrations of H_2S and exposure duration and frequency, which could be utilized to emulate STM and LTM in biological systems.[41] The sensing performance and synaptic behaviors of the device will be evaluated in detail respectively in the following sessions.

2.3. Biomimetic Olfactory Sensing of H_2S Based on the Synaptic Device

To demonstrate the sensing functionality toward H_2S of the biomimetic synapse, we have investigated the transfer curves (**Figure 4**a) and corresponding transconductance (Figure 4b) of the device before and after the exposure to H_2S gas molecules at various concentrations ranging from 5 to 25 ppm (volume to volume (v/v) ratio, with pure N_2 as the balance gas) for 10 min. The drain voltage is fixed at $V_d = -0.2$ V with V_g sweeping from 0.2 to 1.0 V. The blank response (dashed line in Figure 4a,b) is acquired by exposing the device under pure N_2 gas. As the H_2S concentrations increase, the transfer curve gradually shifts to the left and the corresponding V_g that attains the max g_m shifts toward lower voltages with a maximum difference up to 200 mV. Furthermore, the normalized response (NR) of the channel current is also used to evaluate the sensing performance of the device, as shown in Figure 4c. The details of the calculation of NR can be found in the Methodology Section. As the H_2S concentration increases, the corresponding NR increases immediately followed by a slight recovery when H_2S gas is replaced with N_2. Moreover, the device with porous SPE shows higher sensitivity (about three to four times) than that with dense SPE at all H_2S concentrations. For example, after the exposure to 10 ppm H_2S, the NR of the device with porous SPE is 0.27, whereas the device with dense SPE is only 0.07. The enhanced sensitivity induced by porous SPE is likely due to th greatly enhanced surface area for the interaction between
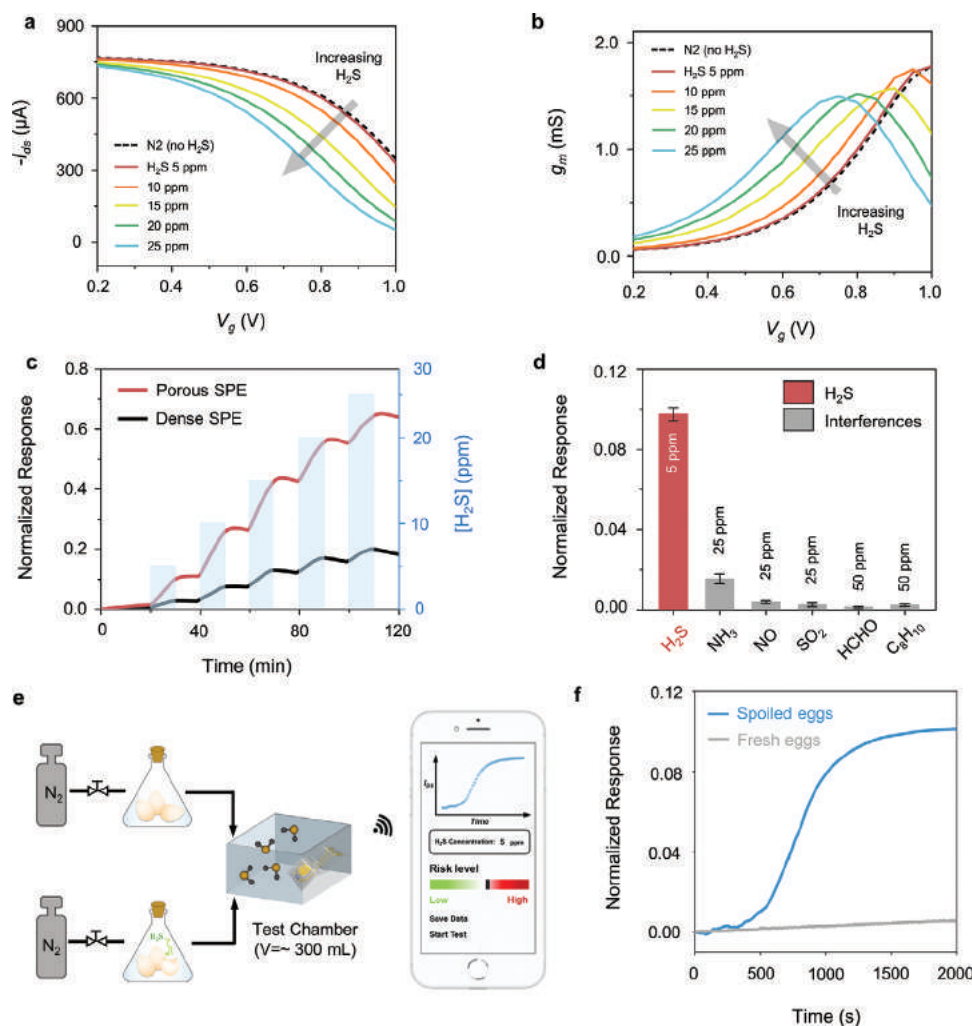
Figure 4. Sensing characteristics of the biomimetic olfactory synapse. a) Transfer characteristics and b) corresponding transconductance curves of the device with different H_2S concentrations sequentially increased from 5 ppm to 25 ppm, with an exposure duration of 10 min at each concentration. c) Real-time normalized response toward H_2S concentrations from 5 to 25 ppm, with an exposure duration of 10 min at each concentration. Drain voltage = −0.2 V, gate bias = 0.4 V. d) Anti-interference performance of the synaptic device toward H_2S over other gas chemicals. e) Schematic illustration of the evaluation of spoiled eggs by detecting the release of H_2S. f) Corresponding real-time normalized current response of fresh and spoiled eggs, respectively.

H_2S molecules and SPE. Porous SPE is therefore adopted for further evaluation of the synaptic device. To evaluate the selectivity toward H_2S of the device, potential interference gases [50 ppm formaldehyde (HCHO), 50 ppm ethylbenzene (C_8H_{10}), 25 ppm sulfur dioxide (SO_2), 25 ppm ammonia (NH_3), and 25 ppm nitric oxide (NO)] are tested with N_2 as the carrier gas. The device demonstrates much greater response toward H_2S than the other gases (Figure 4d), indicating excellent selectivity probably due to the relatively higher solubility of H_2S in [BMIM][TFSI] attributed to the strong interactions between H_2S and [BMIM][TFSI].[42] The photograph of the flexible device on a curved surface is given in Figure S5a (Supporting Information). Consistent normalized responses toward H_2S are obtained of devices in both flat and bent states (Figure S5b, Supporting Information), suggesting desirable flexibility to interface with curvilinear surface. Excellent stability of the device over time (at least 2 weeks) is also demonstrated as shown in Figure S6

(Supporting Information). After storage in air for 2 weeks, the NR toward 5 ppm H_2S retains 91.2% of the original value.

As H_2S is closely associated with rotten food such as eggs and meat, the synaptic device is explored as a potential monitor for food quality through sampling the concentration of H_2S of eggs. A remotely operated and battery-powered circuit module coupled with a custom software package and a Bluetooth is integrated with the synaptic device to enable wireless evaluation. The schematic diagram of the wireless module and the circuit design and system architecture can be found in Figure S7a,b (Supporting Information). As shown in Figure 4e, three eggs are placed in a sealed glass bottle (volume: ≈400 mL) and stored at 30 °C for 2 weeks. Another three fresh eggs are placed in another sealed glass bottom as the control group. The evaluation is performed by flushing the gas in the glass bottles through a carrier gas (N_2) into a gas chamber with the synaptic device. It is noted that the device stays in the gas chamber with

a constant N_2 gas flow to stabilize the initial response before sampling the gas from the eggs. The gas in contact with fresh eggs is first evaluated for 30 min followed by the evaluation of the gas of spoiled eggs for another 30 min and the results are shown in Figure 4f. NR from spoiled eggs is much greater than that of the control group, indicating the detection of significantly higher amount of H_2S. These results suggest that the synaptic device can successfully achieve H_2S sensing wirelessly in practical scenarios.

2.4. Gasotransmitter-Mediated Plasticity of the Synaptic Device

Besides the sensing capability toward H_2S, the PEDOT:PSS device also demonstrates H_2S-mediated synaptic behavior, such as STM and LTM behavior that is often observed in biological synapse.[43] Such memory function can be used to imitate short-term and long-term impacts of H_2S on human olfactory system,

as the associated toxic effects are typically cumulative[44] and dose-dependent.[45] For example, trace amounts of H_2S from short-term exposure can be metabolized by the human body,[46] indicating a STM behavior such as the temporary damage and subsequent repair of epithelial cells.[47] However, frequent exposure to low levels of H_2S can trigger permanent damage (LTM) on the olfactory system (e.g., smell loss).[48]

The results of demonstrated gasotransmitter-mediated plasticity and corresponding STM to LTM behavior of the biomimetic olfactory synapse is shown in **Figure 5** and Figure S8 (Supporting Information). A pulse signal is applied on the gate (V_g = +0.4 V, 30 s) mimicking the input spike in the pre-neuron to trigger the corresponding inhibitory postsynaptic current (IPSC), which is one of the most important synaptic behaviors. In the absence of H_2S stimulus, pulse signals do not affect the amplitude of drain current (I_{ds}) mimicking the IPSC or the changes in channel conductance mimicking the change of synaptic weight (ΔW) (Figure 5a; Figures S8a, and S9,
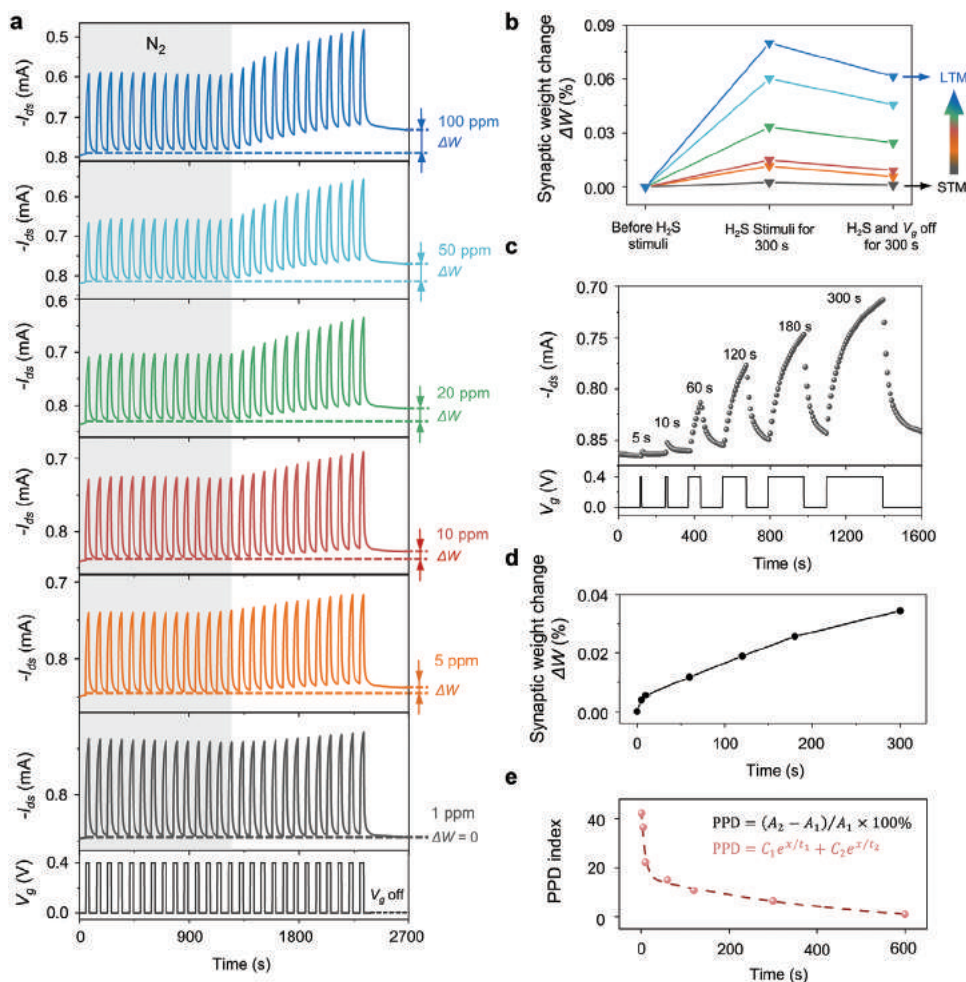

Figure 5. Gasotransmitter-mediated plasticity of the biomimetic olfactory synapse. a) Short-term and long-term conditioning of the biomimetic olfactory synapse with pulsed gate bias (gate voltage = 0.4 V, pulse interval Δt = 60 s, pulse duration $\Delta \tau$ = 30 s). N_2 is introduced for the first 1200 s followed by H_2S stimuli with concentrations varying from 1 to 100 ppm, respectively. ΔW indicates the change of synaptic weight. b) Changes in the synaptic weight (ΔW) before H_2S stimuli, 300 s after H_2S stimuli, and 300 s after the removal of H_2S and V_g, demonstrating STM-to-LTM transition associated with the increase of H_2S concentration. c, Real-time response current (I_{ds}) and d, corresponding synaptic weight changes (ΔW) of the synaptic device as a function of voltage pulse width ranging from 5 to 300 s under the exposure to 20 ppm H_2S. Pulse voltage = 0.4 V. e, Paired pulse depression (PPD) index of the synaptic device. Dotted line shows the fitting result.

**ADVANCED
SCIENCE NEWS**

www.advancedsciencenews.com

**ADVANCED
FUNCTIONAL
MATERIALS**

www.afm-journal.de

Supporting Information). Once H_2S is applied, both the amplitude of channel current (IPSC) and changes in channel conductance (ΔW) increase simultaneously. Specifically, in the presence of trace amounts of H_2S (e.g., 0.2–1 ppm), the channel current first increases and then slowly recovers to the initial current value, resulting in $\Delta W = 0$ after the removal of stimuli (both H_2S and gate pulse) as shown in Figure 5a (grey line) and Figure S8 (Supporting Information), indicating a STM behavior. The H_2S concentrations (0.2–1 ppm) exhibit a linear relationship with the resulted ΔW after H_2S stimuli for 300 s (Figure S8b, Supporting Information). The results suggest a response limit of 200 ppb H_2S and the STM behavior can imitate the metabolization of the human body toward hazardous gases at low concentrations. With the increase of H_2S concentrations, the channel current cannot recover to the initial state, indicating that H_2S-induced synaptic weight changes are stored by the artificial synapse (Figure 5a). The long-lasting ΔW indicates a non-volatile behavior which could emulate the long-term damage of olfactory system upon the excessive exposure of H_2S, also known as LTM. Moreover, the channel current of the device can recover from the exposure of high concentrations (> 1 ppm) of H_2S stimuli by switching off V_d. As shown in Figure S10 (Supporting Information), after exposed in 20 ppm H_2S for 5 pulses, the long-lasting ΔW can be erased by turning off V_d for a short period of time. After turning back on V_d, the channel current recovers to the initial state and the device remains original operational characteristics. Nevertheless, long-lasting ΔW cannot be recovered after being exposed in intensive stimuli (excessive H_2S concentrations, prolonged exposure duration, etc.), which could be utilized to imitate permanent damage.

X-ray photoelectron spectroscopy (XPS) are performed to confirm the retention of cations ([BMIM]$^+$) inside the PEDOT:PSS channel after excessive H_2S exposure mimicking the LTM state. As shown in Figure S11 (Supporting Information), in the absence of H_2S exposure, the post-operation PEDOT:PSS channel shows distinct S $2p$ peaks around 162–165 eV and 166–172 eV corresponding to the PEDOT and PSS phases respectively,[38b] and no F $1s$ or N $1s$ peaks are observed, indicating the electrochemical doping and de-doping process within the PEDOT:PSS channel is reversible (no retention of cations). By contrast, after the operation under H_2S exposure (100 ppm for 20 min), S $2p$ peaks around 162–165 eV are weaker indicating the de-doping of PEDOT:PSS channel, while the N $1s$ peak from the imidazolium ring of [BMIM]$^{+[49]}$ is observed suggesting that some of cations ([BMIM]$^+$) are trapped within the channel due to the ion exchange between the PEDOT$^+$ and [BMIM]$^+$.

Figure 5b summarizes ΔW after the stimulus of H_2S for 300 s and after the removal of both H_2S and pulsed gate voltage for 300 s. With the increase of the concentrations of H_2S (from 5 to 100 ppm), both the ΔW upon H_2S stimulus and the retained ΔW (H_2S and pulsed gate voltage off) increases, indicating that STM gradually transforms to LTM. Based on Hebbian learning theory,[50] an increase in ΔW can also result from persistent stimulation. To demonstrate this behavior, real-time responses of the biomimetic synapse toward 20 ppm H_2S with different pulse durations (5, 10, 60, 120, 180, and 300 s) are investigated (Figure 5c) and the corresponding time-ΔW

relation is shown in Figure 5d. STM-to-LTM transition is successfully demonstrated by tuning the pulse duration. Finally, typical paired-pulse depression (PPD), a type of synaptic plasticity that is vital to decode temporal information in olfactory system,[51] is also evaluated in the artificial synapse (Figure 5e). A pair of presynaptic gate spikes trigger two peak channel currents, and the second peak is larger than the former one. However, when the pulse interval between two presynaptic spikes is shorter, the difference between two current peaks becomes greater. Such PPD behavior can be described by a double-exponential function (Figure 5e). As shown in Figure 5e, the PPD index increases while the pulse interval decreases, which is similar to the behavior of a biological synapse.[52] The gasotransmitter-mediated plasticity of the device modulated by H_2S pulses is also investigated. As shown in Figure S12 (Supporting Information), five consecutive H_2S pulses (1, 2, 5, and 10 ppm) with a pulse width of 60 s and an interval time of 60 s are applied to the device, at a constant V_g (+0.4 V). As shown in Figure S12 (Supporting Information), the inhibitory current gradually increases over time upon H_2S pulses. The increase of current slows down when H_2S is removed and is expected to reach a plateau and even slowly recover if sufficient time is given, as shown in Figure 4c. The phenomenon is attributed to the de-doping process of PEDOT:PSS-based OECTs, in which the current response is accumulative as long as V_g remains ON and the current inhibiting effect becomes more significant with increasing pulse number and H_2S concentrations. These results demonstrate the gas accumulative effect modulated by gas pulses and concentrations. In addition, measured gate leakage currents are lower than 30 nA (Figure S13, Supporting Information) during the tests of synaptic behaviors, indicating a reliable device operation.

In all, the interaction of H_2S molecules with SPE and subsequent doping/de-doping of PEDOT:PSS channel endows the proposed biomimetic synapse with interesting sensing and memorizing capabilities toward H_2S imitating biological synaptic functions. Compared with conventional gas sensors, the synaptic device enables an integrated system with on-board functions of sensing and memorizing, and allows real-time monitoring of accumulative effects of target gases. The proposed device could therefore be applied for alarming dangerous circumstances when hazardous trace gases accumulate to a certain level, which is of great importance for intelligent artificial olfactory systems.

3. Discussion

We propose a flexible and biomimetic olfactory synapse based on an all-solid-state OECT device with porous SPE fabricated by a breath-figure method. The synaptic device shows excellent sensitivity (ppb-level) and selectivity toward H_2S over other interfering gases including HCHO, C_8H_{10}, SO_2, NH_3, and NO (Table S1, Supporting Information). Coupled with a wireless system, the biomimetic olfactory synapse accomplishes the detection of excessive concentrations of H_2S of rotten eggs. Representative synaptic behaviors, including IPSC, PPD, STM, LTM and transition from STM to LTM are successfully demonstrated. More intriguing, the proposed device enables

the emulation of cumulative damage caused by H_2S exposure under different concentrations, durations, and frequency. The channel geometry of PEDOT (i.e., channel dimensions and gate area) has been reported to affect device characteristics.[34b,53] For example, channel length plays an important role in device sensitivity, response time and operational voltage, and the capacitance ratio of the channel to the gate affects gating efficiency. Future optimization of channel geometry will therefore be essential to achieve miniaturized, fast-response and highly sensitive olfactory synapse. The implementation of different SPE for independent gating could allow synapse arrays that mimic the complicated olfactory system for multiple odors detection and recognition. Combined with algorithms of neural network, smart biomimetic olfactory platforms could be possible. This research opens new routes toward advanced artificial olfactory systems that could enable simultaneous sensing and synaptic functions in an all-in-on device and set an essential foundation for intelligent healthcare.

4. Experimental Section

Device Fabrication: Devices were fabricated by the following process including electrodes deposition, patterning of PEDOT:PSS channel, SU-8 passivation, and SPE drop casting. Au electrodes (5 nm Cr/100 nm Au) were first deposited by magnetron sputtering and patterned through photolithography to realize source, drain, and gate contacts on a flexible PET substrate (125 μm). The PEDOT:PSS channel was patterned by photolithography and reactive oxygen etching (RIE). Specifically, PEDOT precursor dispersion (Clevios PH-1000) was spin-coated on the PET substrate (500 rpm/6 s, 2500 rpm/40 s), followed by baking at 120 °C for 1 h. Ethylene glycol (10 volume%, AR, Beijing Lanyi chemical products Co., Ltd), Dodecylbenzene sulfonate (0.1 volume%, Shanghai Aladdin Bio-Chem Technology Co., Ltd), and (3-glycidyloxypropyl)trimethoxysilane (1 wt.%, J&K Scientific Ltd) were added into the PEDOT:PSS dispersion to improve conductivity and film stability. Photolithography was performed with negative photoresist (AZ nLOF 2070, 500 rpm/5 s, 3000 rpm/30). Final patterns of PEDOT:PSS was achieved through RIE (90 mTorr pressure, 100 sccm O_2, 5 sccm SF_6, power 100 W for 120 s). The device was then encapsulated by a layer of photoresist (SU-8 3005). To obtain the SPE, PVDF-HFP (Sigma-Aldrich) was dissolved in a mixture of DMF (Sigma-Aldrich) and acetone (J&K Scientific Ltd) at 60 °C in a 1:10 mass ratio and the solution was stirred with a magnetic stirrer at 500 rpm before adding [BMIM][TFSI] in a 2:1 ([BMIM][TFSI]: PVDF-HFP) mass ratio. The mixture was stirred at 60 °C for at least 1 h, followed by spin-coating on the PEDOT:PSS device (2000 rpm, 40 s). To obtain the porous structure, the relative humidity was maintained at ≈60% during the spin-coating and solvent evaporation process. The device was thermally annealed at 50 °C in vacuum for 3 h to finish the fabrication process.

Characterization of SPE: SEM images were obtained using an Auriga SEM/FIB Crossbeam System (ZEISS, Germany) at an accelerating voltage of 15 kV. FTIR measurements were performed on a Nicolet 6700 (Thermo Fisher Scientific, USA) in the range of 600–4000 cm^{-1}. XRD measurements were performed using a diffractometer (Rigaku D/max 2500 PC, Japan) with Cu Kα radiation. XPS experiments were conducted on ESCALAB 250Xi (Thermal Fisher, USA).

Wireless Module: The wireless data transmission system consists of four analytical modules: 1) a digital-to-analog converter (DAC) to control V_g and V_{ds}. 2) Two trans-impedance amplifiers (TIA) and a successive approximation register analog-to-digital converter (SAR ADC) to control output voltage and convert collected I_{ds} and I_g to voltage values. 3) A microprogrammed control unit (MCU) controlling DAC, TIA, SAR ADC for specific functions. 4) A customized iOS-based software to realize wireless data exchange and transmission with mobiles based on the Bluetooth module. The size of the wireless system is ≈3.5 cm × 2.5 cm.

Device Characterization: The electrical characteristics of the synaptic device was performed by two Keithley 2400 parameter analyzers. For the testing of output curves, V_g varied from 0 to +1.6 V with a step of +400 mV while V_d was swept from 0 to –0.6 V. For the testing of transfer curves V_g was swept from 0 to 1.5 V with a step of 50 mV while V_d was fixed at –0.2 V. The transconductance was calculated from the corresponding transfer curve according to the equation:

$$g_m = \Delta I_{ds}/\Delta V_g \tag{2}$$

For gas sensing tests, the OECT-based synaptic device was stored in an airtight test chamber (≈ 300 mL). A mixture of N_2 (carrier gas) and H_2S with various concentrations (from 5 to 25 ppm) was introduced into the test chamber using a gas generation and testing system (TC Air Technology Limited Company, Beijing, China). The test started with introducing N_2 into the test chamber for 10 min. After the drain current (I_{ds}) became stable, the mixed gas (N_2 and H_2S) with a target concentration was introduced into the chamber for 10 min in sequence. The anti-interference test was performed with potential interfering chemicals, including 50 ppm HCHO, 50 ppm C_8H_{10}, 25 ppm SO_2, 25 ppm NH_3, and 25 ppm NO, with N_2 as the carrier gas.

The normalized response of the device was calculated from the recorded drain current by following equations:[54]

$$NR = \left| I_{ds}^{gas} - I_{ds}^{0} \right| / I_{ds}^{0} \tag{3}$$

where I_{ds}^{gas} is the drain current of the device upon the exposure to different testing gases and I_{ds}^{0} is the drain current of the device in the N_2.

To detect H_2S released from eggs, two air tight glass bottles containing three eggs were prepared. One bottle contains fresh eggs while the other contains spoiled eggs which had been stored at 30 °C for two weeks. N_2 was used as the carried gas to flush the gas from the two bottles to a test chamber for investigation. The gas from the bottle containing fresh eggs was sampled first for 30 min, followed by sampling the gas from the bottles containing spoiled eggs for another 30 min. The drain current was recorded by a wireless control and data transmission system.

To evaluate gas-mediated synapse plasticity, the short-term and long-term conditioning of the synaptic device was characterized with successive presynaptic voltage pulses (ΔV_g = +0.4 V, pulse length = 30 s, pulse interval = 60 s) and the postsynaptic current (I_{ds}) was monitored. During the measurement, N_2 was introduced into the test chamber for the first 14 gate pulses, followed by the introduction of H_2S at different concentrations in sequence. After 26 IPSCs, the gate pulses and the H_2S were turned off. The initial current (before the first presynaptic pulse) and the current after the last presynaptic pulse were defined as W_0 and W_n, respectively. The changes in the synaptic weight (ΔW) was calculated based on $\Delta W = W_n - W_0$. To investigate the influence of pulse duration on ΔW, various presynaptic pulses (ΔV_g = +0.4 V, pulse interval = 60 s) with different pulse durations ranging from 5 to 300 s and 20 ppm H_2S were applied. The PPD behavior was investigated by applying a pair of presynaptic gate spikes and the postsynaptic current (I_{ds}) was recorded. The first and the second postsynaptic current peaks were denoted as A_1 and A_2, respectively. The PPD index was then calculated to obtain PPD index = $(1 - A_2/A_1) \times 100\%$. The hole mobility that reflects the electronic transport of PEDOT:PSS channel was obtained by time of flight measurement. Specifically, a constant gate current (I_g) s applied to the device for 5 s and corresponding I_{ds} as a function of time was recorded. According to Bernards model,[38a] the simplified transient behavior can be described by the equation of $I(t,I_g)_{ds} = I_O - I_g\left(f + \dfrac{t}{\tau_e}\right)$, where f is a constant and I_O is the channel current prior to the application of a gate current. The current changes during the first and fifth seconds were used to plot the slope of the source/drain transient as a function of gate current. The hole transit time (τ_e) was obtained based on the equation of $dI_{ds}/dt = -I_g/\tau_e$ and the hole drift mobility was calculated based on $\mu = L^2/V_{ds}\tau_e$, where L is the PEDOT:PSS channel length.

Supporting Information

Supporting Information is available from the Wiley Online Library or from the author.

Acknowledgements

Conflict of Interest

The authors declare no conflict of interest.

Data Availability Statement

The data that supports the findings of this study are available in the supplementary material of this article.

Keywords

[1] V. M. Ho, J.-A. Lee, K. C. Martin, *Science* **2011**, *334*, 623.

[2] J. Zhu, T. Zhang, Y. Yang, R. Huang, *Appl. Phys. Rev.* **2020**, *7*, 011312.

[3] a) F. Sun, Q. Lu, S. Feng, T. Zhang, *ACS Nano* **2021**, *15*, 3875; b) Y. Xu, W. Liu, Y. Huang, C. Jin, B. Zhou, J. Sun, J. Yang, *Adv. Electron. Mater.* **2021**, *7*, 2100336.

[4] Y. He, Y. Yang, S. Nie, R. Liu, Q. Wan, *J. Mater. Chem. C* **2018**, *6*, 5336.

[5] a) L. Liu, W. Xu, Y. Ni, Z. Xu, B. Cui, J. Liu, H. Wei, W. Xu, *ACS Nano* **2022**, *16*, 2282; b) Y. Lee, Y. Liu, D.-G. Seo, J. Y. Oh, Y. Kim, J. Li, J. Kang, J. Kim, J. Mun, A. M. Foudeh, Z. Bao, T.-W. Lee, *Nat. Biomed. Eng.* **2022**, https://doi.org/10.1038/s41551-022-00918-xv; c) Y. Wang, D. Liu, Y. Zhang, L. Fan, Q. Ren, S. Ma, M. Zhang, *ACS Nano* **2022**, *16*, 8283; d) J. Gong, H. Wei, J. Liu, L. Sun, Z. Xu, H. Huang, W. Xu, *Matter* **2022**, *5*, 1578; e) S. Oh, J.-I. Cho, B. H. Lee, S. Seo, J.-H. Lee, H. Choo, K. Heo, S. Y. Lee, J.-H. Park, *Sci. Adv.* **2021**, *7*, abg9450; f) H. Shim, S. Jang, A. Thukral, S. Jeong, H. Jo, B. Kan, S. Patel, G. Wei, W. Lan, H.-J. Kim, C. Yu, *Proc. Natl. Acad. Sci. USA* **2022**, *119*, 2204852119.

[6] a) S. Seo, S.-H. Jo, S. Kim, J. Shim, S. Oh, J.-H. Kim, K. Heo, J.-W. Choi, C. Choi, S. Oh, D. Kuzum, H. S. P. Wong, J.-H. Park, *Nat. Commun.* **2018**, *9*, 5106; b) J. Yu, X. Yang, G. Gao, Y. Xiong, Y. Wang, J. Han, Y. Chen, H. Zhang, Q. Sun, Z. L. Wang, *Sci. Adv.* **2021**, *7*, abd9117; c) S. M. Kwon, S. W. Cho, M. Kim, J. S. Heo, Y.-H. Kim, S. K. Park, *Adv. Mater.* **2019**, *31*, 1906433; d) X. Geng, L. Hu,

F. Zhuge, X. Wei, *Adv. Intell. Syst.* **2022**, *4*, 2200019; e) F. Zhou, Z. Zhou, J. Chen, T. H. Choy, J. Wang, N. Zhang, Z. Lin, S. Yu, J. Kang, H. S. P. Wong, Y. Chai, *Nat. Nanotechnol.* **2019**, *14*, 776.

[7] a) C. Wan, P. Cai, X. Guo, M. Wang, N. Matsuhisa, L. Yang, Z. Lv, Y. Luo, X. J. Loh, X. Chen, *Nat. Commun.* **2020**, *11*, 4602; b) H. Tan, Y. Zhou, Q. Tao, J. Rosen, S. van Dijken, *Nat. Commun.* **2021**, *12*, 1120; c) Q. Duan, T. Zhang, C. Liu, R. Yuan, G. Li, P. Jun Tiw, K. Yang, C. Ge, Y. Yang, R. Huang, *Adv. Intell. Syst.* **2022**, *4*, 2200039.

[8] a) Y. Li, K. Yin, Y. Diao, M. Fang, J. Yang, J. Zhang, H. Cao, X. Liu, J. Jiang, *Nanoscale* **2022**, *14*, 2316; b) G. Feng, J. Jiang, Y. Li, D. Xie, B. Tian, Q. Wan, *Adv. Funct. Mater.* **2021**, *31*, 2104327.

[9] a) C. Sarafoleanu, C. Mella, M. Georgescu, C. Perederco, *J. Med. Life* **2009**, *2*, 196; b) C. Kim, K. K. Lee, M. S. Kang, D.-M. Shin, J.-W. Oh, C.-S. Lee, D.-W. Han, *Biomater. Res.* **2022**, *26*, 40; c) T. Wang, H.-M. Huang, X.-X. Wang, X. Guo, *InfoMat* **2021**, *3*, 804; d) J.-K. Han, M. Kang, J. Jeong, I. Cho, J.-M. Yu, K.-J. Yoon, I. Park, Y.-K. Choi, *Adv. Sci.* **2022**, *9*, 2106017.

[10] C.-Y. Su, K. Menuz, J. R. Carlson, *Cell* **2009**, *139*, 45.

[11] a) C. Wu, Y.-W. Du, L. Huang, Y. Ben-Shoshan Galeczki, A. Dagan-Wiener, M. Naim, M. Y. Niv, P. Wang, *Sensors* **2017**, *17*, 2881; b) J. H. Brann, S. J. Firestein, *Front. Neurosci.* **2014**, *8*, 182.

[12] a) H. Kaba, S. Nakanishi, *Rev. Neurosci.* **1995**, *6*, 125; b) D. Wilson, A. Best, R. Sullivan, *Neuroscientist* **2004**, *10*, 513.

[13] a) M. I. Abdel-Aziz, P. Brinkman, S. J. H. Vijverberg, A. H. Neerincx, R. de Vries, Y. W. F. Dagelet, J. H. Riley, S. Hashimoto, P. Montuschi, K. F. Chung, R. Djukanovic, L. J. Fleming, C. S. Murray, U. Frey, A. Bush, F. Singer, G. Hedlin, G. Roberts, S.-E. Dahlén, I. M. Adcock, S. J. Fowler, K. Knipping, P. J. Sterk, A. D. Kraneveld, A. H. Maitland-van der Zee, *J. Allergy Clin. Immunol.* **2020**, *146*, 1045; b) D. K. Nurputra, A. Kusumaatmaja, M. S. Hakim, S. N. Hidayat, T. Julian, B. Sumanto, Y. Mahendradhata, A. M. I. Saktiawati, H. S. Wasisto, K. Triyana, *npj Digital Med.* **2022**, *5*, 115; c) O. S. Kwon, H. S. Song, S. J. Park, S. H. Lee, J. H. An, J. W. Park, H. Yang, H. Yoon, J. Bae, T. H. Park, J. Jang, *Nano Lett.* **2015**, *15*, 6559.

[14] a) Z. Song, Y. Tong, X. Zhao, H. Ren, Q. Tang, Y. Liu, *Mater. Horiz.* **2019**, *6*, 717; b) Y. Chu, H. Tan, C. Zhao, X. Wu, S.-J. Ding, *ACS Appl. Mater. Interfaces* **2022**, *14*, 9368.

[15] a) X. Ji, B. D. Paulsen, G. K. K. Chik, R. Wu, Y. Yin, P. K. L. Chan, J. Rivnay, *Nat. Commun.* **2021**, *12*, 2480; b) C. Lubrano, U. Bruno, C. Ausilio, F. Santoro, *Adv. Mater.* **2022**, *34*, 2110194.

[16] a) P. Gkoupidenis, N. Schaefer, B. Garlan, G. G. Malliaras, *Adv. Mater.* **2015**, *27*, 7176; b) H. Shu, H. Long, H. Sun, B. Li, H. Zhang, X. Wang, *ACS Omega* **2022**, *7*, 14622.

[17] P. Gkoupidenis, D. A. Koutsouras, G. G. Malliaras, *Nat. Commun.* **2017**, *8*, 15448.

[18] a) J. C. Perez, S. E. Shaheen, *MRS Bull.* **2020**, *45*, 649; b) S.-K. Lee, Y. W. Cho, J.-S. Lee, Y.-R. Jung, S.-H. Oh, J.-Y. Sun, S. Kim, Y.-C. Joo, *Adv. Sci.* **2021**, *8*, 2001544.

[19] a) W. Guo, J.-t. Kan, Z.-y. Cheng, J.-f. Chen, Y.-q. Shen, J. Xu, D. Wu, Y.-z. Zhu, *Oxid. Med. Cell. Longev.* **2012**, *2012*, 878052; b) J. Pant, A. Mondal, J. Manuel, P. Singha, J. Mancha, H. Handa, *ACS Biomater. Sci. Eng.* **2020**, *6*, 2062.

[20] a) C. Zhang, K. Wu, H. Liao, M. Debliquy, *Chem. Eng. J.* **2022**, *430*, 132813; b) M. J. Bezdek, S.-X. L. Luo, R. Y. Liu, Q. He, T. M. Swager, *ACS Cent. Sci.* **2021**, *7*, 1572; c) Q. Xu, B. Zong, Q. Li, X. Fang, S. Mao, K. Ostrikov, *J. Hazard. Mater.* **2022**, *424*, 127492.

[21] a) A. R. Hirsch, G. Zavala, *Occup. Environ. Med.* **1999**, *56*, 284; b) M. G. Costigan, *Occup. Environ. Med.* **2003**, *60*, 308.

[22] a) A. Zhang, H. Bai, L. Li, *Chem. Rev.* **2015**, *115*, 9801; b) X. Zhang, B. Wang, L. Huang, W. Huang, Z. Wang, W. Zhu, Y. Chen, Y. Mao, A. Facchetti, T. J. Marks, *Sci. Adv. 6*, eaaz1042.

[23] M. Abreha, A. R. Subrahmanyam, J. S. Kumar, *Chem. Phys. Lett.* **2016**, *658*, 240.

[24] P. K. Singh, K. C. Sabin, X. Chen, *Polym. Bull.* **2016**, *73*, 255.

[25] a) C.-C. Yang, H.-Y. Lin, A. Kumar, B. Pattanayak, H.-Y. Tsai, T. Winie, T.-Y. Tseng, *RSC Adv.* **2018**, *8*, 30239; b) Shalu, V. K. Singh, R. K. Singh, *J. Mater. Chem. C* **2015**, *3*, 7305.

[26] a) J. Ko, X. Wu, A. Surendran, B. T. Muhammad, W. L. Leong, *ACS Appl. Mater. Interfaces* **2020**, *12*, 33979; b) A. Weissbach, L. M. Bongartz, M. Cucchi, H. Tseng, K. Leo, H. Kleemann, *J. Mater. Chem. C* **2022**, *10*, 2656.

[27] a) P. Tamilarasan, S. Ramaprabhu, *Energy* **2013**, *51*, 374; b) S. Bovio, A. Podestà, C. Lenardi, P. Milani, *J. Phys. Chem. B* **2009**, *113*, 6600.

[28] a) J. P. Tafur, A. J. Fernández Romero, *J. Membr. Sci.* **2014**, *469*, 499; b) W. Liu, C. Yi, L. Li, S. Liu, Q. Gui, D. Ba, Y. Li, D. Peng, J. Liu, *Angew. Chem., Int. Ed.* **2021**, *60*, 12931.

[29] M. Herstedt, M. Smirnov, P. Johansson, M. Chami, J. Grondin, L. Servant, J. C. Lassègues, *J. Raman Spectrosc.* **2005**, *36*, 762.

[30] S. K. Chaurasia, R. K. Singh, S. Chandra, *J. Polym. Sci., Part B: Polym. Phys.* **2011**, *49*, 291.

[31] A. V. Volkov, K. Wijeratne, E. Mitraka, U. Ail, D. Zhao, K. Tybrandt, J. W. Andreasen, M. Berggren, X. Crispin, I. V. Zozoulenko, *Adv. Funct. Mater.* **2017**, *27*, 1700329.

[32] A. P. Sandoval, J. M. Feliu, R. M. Torresi, M. F. Suárez-Herrera, *RSC Adv.* **2014**, *4*, 3383.

[33] a) Z. Yi, G. Natale, P. Kumar, E. D. Mauro, M.-C. Heuzey, F. Soavi, I. I. Perepichka, S. K. Varshney, C. Santato, F. Cicoira, *J. Mater. Chem. C* **2015**, *3*, 6549; b) V. Kaphle, S. Liu, C.-M. Keum, B. Lüssem, *Phys. Status Solidi A* **2018**, *215*, 1800631.

[34] a) J. Rivnay, P. Leleux, M. Sessolo, D. Khodagholy, T. Herve, M. Fiocchi, G. G. Malliaras, *Adv. Mater.* **2013**, *25*, 7010; b) D. Khodagholy, J. Rivnay, M. Sessolo, M. Gurfinkel, P. Leleux, L. H. Jimison, E. Stavrinidou, T. Herve, S. Sanaur, R. M. Owens, G. G. Malliaras, *Nat. Commun.* **2013**, *4*, 2133.

[35] a) A. Afsharpour, *Chin. J. Chem. Eng.* **2022**, *44*, 521; b) A. Boruń, A. Bald, *Ionics* **2016**, *22*, 859.

[36] a) A. Deshpande, L. Kariyawasam, P. Dutta, S. Banerjee, *J. Phys. Chem. C* **2013**, *117*, 25343; b) F. Li, A. Laaksonen, X. Zhang, X. Ji, *Ind. Eng. Chem. Res.* **2022**, *61*, 2643.

[37] a) Y. Wang, X. Liu, A. Kraslawski, J. Gao, P. Cui, *J. Cleaner Prod.* **2019**, *213*, 480; b) R. Santiago, J. Lemus, A. X. Outomuro, J. Bedia, J. Palomar, *Sep. Purif. Technol.* **2020**, *233*, 116050.

[38] a) D. A. Bernards, G. G. Malliaras, *Adv. Funct. Mater.* **2007**, *17*, 3538; b) X. Wu, M. Stephen, T. C. Hidalgo, T. Salim, J. Surgailis, A. Surendran, X. Su, T. Li, S. Inal, W. L. Leong, *Adv. Funct. Mater.* **2022**, *32*, 2108510.

[39] S. T. Keene, T. P. A. van der Pol, D. Zakhidov, C. H. L. Weijtens, R. A. J. Janssen, A. Salleo, Y. van de Burgt, *Adv. Mater.* **2020**, *32*, 2000270.

[40] B. Zhou, W. Liu, Y. Xu, C. Jin, J. Yang, J. Sun, *J. Phys. D: Appl. Phys.* **2022**, *55*, 304006.

[41] R. M. Shiffrin, R. C. Atkinson, *Psychol. Rev.* **1969**, *76*, 179.

[42] a) Z. Lei, C. Dai, B. Chen, *Chem. Rev.* **2014**, *114*, 1289; b) C. Chiappe, C. S. Pomelli, *Top. Curr. Chem.* **2017**, *375*, 52.

[43] T. Ohno, T. Hasegawa, T. Tsuruoka, K. Terabe, J. K. Gimzewski, M. Aono, *Nat. Mater.* **2011**, *10*, 591.

[44] B. Skrajny, R. J. Reiffenstein, R. S. Sainsbury, S. H. Roth, *Toxicol. Lett.* **1996**, *84*, 43.

[45] H. A. -L. Mousa, *Environ. Health Prev. Med.* **2015**, *20*, 12.

[46] a) H. Kimura, *Front. Physiol.* **2012**, *3*, 101; b) N. Zaichko, A. Melnik, M. Yoltukhivskyy, A. Olhovskiy, I. Palamarchuk, *Ukr. Biochem. J.* **2014**, *86*, 5.

[47] D. C. Dorman, M. F. Struve, E. A. Gross, K. A. Brenneman, *Toxicol. Appl. Pharmacol.* **2004**, *198*, 29.

[48] T. L. Guidotti, *Int. J. Toxicol.* **2010**, *29*, 569.

[49] S. Seo, J. Park, Y.-C. Kang, *Bull. Korean Chem. Soc.* **2016**, *37*, 355.

[50] D. Hebbs, *The Organization of Behavior: A Neuropsychological Theory*, Wiley and Sons, New York, NY, USA **1949**, https://doi.org/10.1002/sce.37303405110.

[51] a) S. Liu, *Front. Cell. Neurosci.* **2020**, *14*, 181; b) S. I. Cohen-Matsliah, Y. Seroussi, K. Rosenblum, E. Barkai, *Learn. Mem.* **2008**, *15*, 756.

[52] R. S. Zucker, W. G. Regehr, *Annu. Rev. Physiol.* **2002**, *64*, 355.

[53] J. Rivnay, P. Leleux, M. Sessolo, D. Khodagholy, T. Hervé, M. Fiocchi, G. G. Malliaras, *Adv. Mater.* **2013**, *25*, 7010.

[54] D. A. Bernards, D. J. Macaya, M. Nikolou, J. A. DeFranco, S. Takamatsu, G. G. Malliaras, *J. Mater. Chem.* **2008**, *18*, 116.